Removal of Instantaneous Reactive Power From High-Conversion-Ratio Bidirectional Resonant Converter With Balanced Capacitor Voltage

Sungho Son, *Member, IEEE*, Hwasoo Seok, *Student Member, IEEE*, and Minsung Kim, *Member, IEEE*

***Abstract*—This article presents bidirectional operation of a resonant converter that features high step-up/down capability, high efficiency, and balanced capacitor voltage. When transferring power in the backward direction, the original converter may suffer from significant reverse current due to large fluctuation of the resonant capacitor voltage. By applying the right amount of phase in the pulsewidth-modulation signal, we can remove the instantaneous reactive power generated during the backward operation. We first derive the nominal duty ratio of the secondary side in terms of the backward voltage gain, then derive the threshold load level, above which the instantaneous reactive power appears, and compute the required amount of phase shift to remove it. We also analyze the sensitivity of the required amount of phase with regard to resonant tank parameters. A 400-W prototype converter has been built to demonstrate the performance of the proposed converter.**

***Index Terms*—Bidirectional operation, capacitor voltage balancing, duality, energy storage system (ESS), high step-up/down, instantaneous reactive power, phase adjustment.**

I. Introduction

INTEGRATION of small/medium size energy storage systems (ESSs) allows a wide variety of distributed grid applications requiring different power capacities [1]–[3]. In fact, they are widely incorporated in a light-weight electric vehicle and electric scooter applications [4], [5]. Naturally, these ESSs contain a number of low-voltage battery cells. To provide an interface between the low-voltage battery (12–48 V) and the high-voltage dc bus (380 V or higher), we need to use a high-voltage conversion ratio bidirectional dc–dc converter.

Manuscript received December 1, 2019; revised February 17, 2020; accepted March 19, 2020. Date of publication March 29, 2020; date of current version July 20, 2020. This research was supported in part by Basic Science Research Program through the National Research Foundation of Korea (NRF) funded by the Ministry of Education under Grant 2018R1D1A1B07044999 and in part by the Ministry of Science and ICT (MSIT), Korea, under the ICT Consilience Creative Program (IITP-2019-2011-1-00783) supervised by the Institute for Information & Communications Technology Planning & Evaluation (IITP). Recommended for publication by Associate Editor J. Marcos Alonso. *(Corresponding author: Minsung Kim.)*

Sungho Son is with the Coil Power Supply Section, ITER Organization, St. Paul-lez-Durance 13115, France (e-mail: sungho.son@iter.org).

Hwasoo Seok is with the Department of Creative IT Engineering, Pohang University of Science and Technology (POSTECH), Pohang 37673, Korea (e-mail: aeinla@postech.ac.kr).

Minsung Kim is with the Division of Electronics and Electrical Engineering, Dongguk University, Seoul 04620, South Korea (e-mail: mkim@dgu.ac.kr).

Color versions of one or more of the figures in this article are available online at http://ieeexplore.ieee.org.

Digital Object Identifier 10.1109/TPEL.2020.2982969

The bidirectional flyback converters are one of the attractive solutions for small/medium size ESS applications because they are simple in structure, equipped with buck-boost capability, and can be built with a lower number of power components. Unfortunately, the leakage inductor of the transformer causes switching loss from the power switches and the output diode suffers from serious reverse-recovery problems, which degrades conversion efficiency. To solve these problems, the flyback converters that use an active-clamp circuit have been proposed in [6]. The energy stored in the leakage and the magnetizing inductances of the transformer is recycled, and all of the primary switches can achieve zero-voltage-switching (ZVS) turn-ON. A zero-current-switching (ZCS) bidirectional flyback converter is proposed in [7]. By adding an auxiliary winding in the coupled inductor, it achieves ZCS for all power switches and diodes, thereby reducing switching losses and voltage stresses. Delshad *et al.* [8] also proposed ZCS bidirectional flyback converters that can achieve soft-switching without introducing extra switches. To achieve a high voltage conversion ratio, a bidirectional flyback topology-based parallel-input series-output converter has been proposed in [9]. The energy stored in leakage inductance can be recycled by a dual-inductor-capacitor-diode snubber instead of traditional resistor-capacitor-diode snubbers, which yields further efficiency improvement. However, these bidirectional flyback converters must operate with extremely high duty ratio to achieve a very high voltage conversion ratio. Operating under an extremely high duty cycle may result in serious reverse-recovery and electromagnetic interference problems. The converters proposed in [10], [11] achieve a high voltage conversion ratio by using a high turns-ratio transformer, but it suffers from large leakage inductance and parasitic capacitances that can cause high voltage or current spikes on the power devices.

Current-fed dual half-bridge converters [12]–[19] are also able to meet most of the requirements for medium-to-low power battery applications. They use only four active power components for bidirectional power transfer. By employing input-side inductors, they operate as boost converters in the forward direction and buck converters in the backward direction. These current-fed converters attain ZVS operation in both forward and backward power flow directions. However, the leakage inductor of the transformer causes high voltage spikes and switching losses from the power switches. To recycle the leakage energy and clamp the voltage stress of power switches, the use of active-clamp circuit has been proposed in [16]. A ZCS current-fed

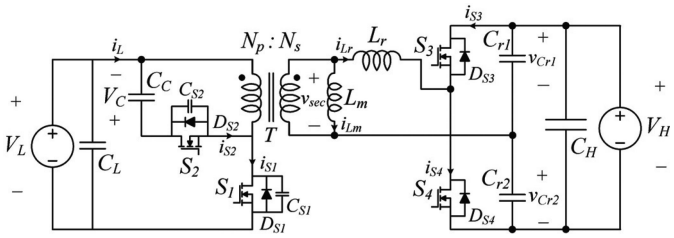

Fig. 1. Circuit diagram of the proposed bidirectional resonant converter. $S_{i'}$, $D_{S'i'}, C_{S'j'}$ $(i = 1, \ldots, 4, j = 1, 2)$: Equivalent models of the switches, where $S_{i'}$ is an ideal switch, $D_{S'i'}$ is a body diode, and $C_{S'j'}$ is a junction capacitor; C_L: A low-side capacitor; C_H: A high-side capacitor; V_C: Voltage across C_c; v_{sec}: Secondary-side voltage of T; v_{Cr1} and v_{Cr2}: Voltages across C_{r1} and C_{r2} respectively; $i_{S'i'}$: Current through the switches S_i $(i = 1, \ldots, 4)$; i_{Lm}: Magnetizing current; i_{Lr}: Current through L_r.

half-bridge isolated dc/dc converter has been proposed in [18]. The modulation of secondary switches clamps the voltage across the primary-side devices and eliminates voltage spike of the switch at turn-OFF instant without any additional components. The ZCS of the primary switches, the natural commutation of secondary diodes, and the zero-current turn-ON of secondary switches are also achieved, resulting in low switching losses. However, they suffer from high voltage stress on the upper capacitor at the primary side and on one of the capacitors at the secondary side.

The converter [20] addressed a unidirectional high step-up resonant dc–dc converter with balanced capacitor voltage. They fixed the duty cycle D_{pri} of the primary-side switches to 0.5, thereby balancing the capacitors in the secondary side regardless of the input voltage and load variations. Switches are used on the secondary side of the circuit instead of diodes; the duty cycle D_{sec} of the secondary-side switches is then controlled to boost the resonant inductor current. We can continue to use the same circuit for the power transfer in the backward direction thanks to its inherent secondary-side switches. In the backward direction, the same $D_{\text{pri}} = 0.5$ should be used for the capacitor voltage balance; the duty cycle of the secondary-side switches is controlled but with different switching sequences. One nontrivial problem is that, if the load increases and exceeds the threshold, the resonant capacitor voltage may fluctuate seriously and turn on the body diodes of the secondary-side switches eventually, thereby causing the reverse current to flow through them. It significantly reduces the power conversion efficiency, which prevents the converter from use in practical battery applications.

To overcome the aforementioned problem, we propose to use a phase adjustment technique to remove the reverse current for a high-conversion-ratio bidirectional resonant converter with balanced capacitor voltage. By applying the right amount of phase in the pulsewidth-modulation (PWM) signal, we are able to remove the instantaneous reactive power generated during the backward operation. Integrating this technique with the one in [20], we can achieve a high conversion ratio in both forward and backward directions. We first derive the nominal duty ratio of the secondary side, then derive the threshold load level, above which the instantaneous reactive power appears, and compute the required amount of phase shift to remove it. We also analyze the sensitivity of the required amount of phase with regard to

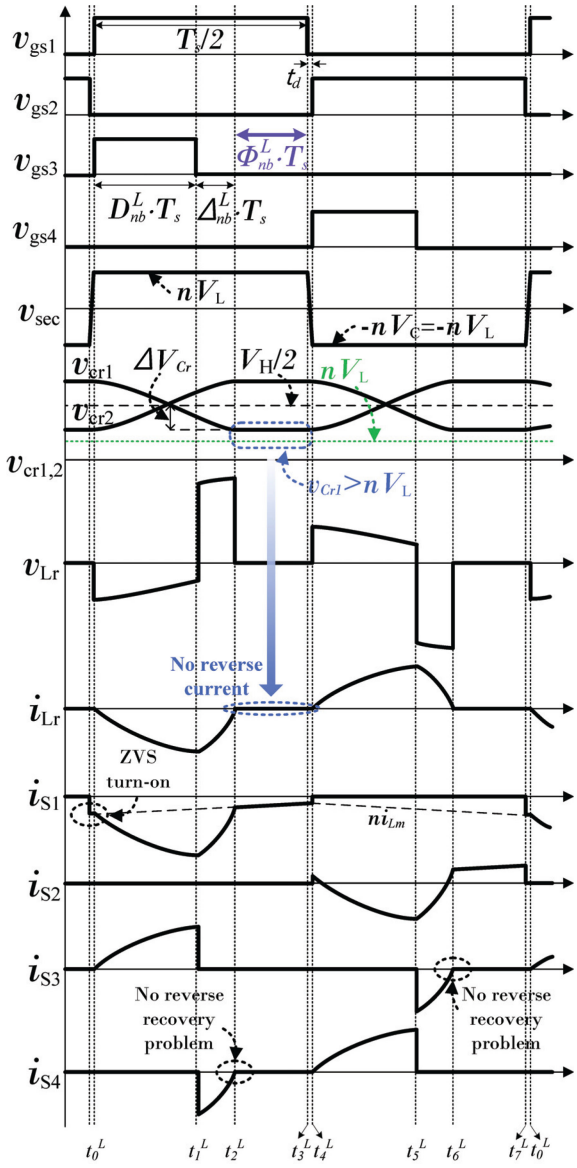

Fig. 2. Voltage, current, and switch waveforms for backward operation with left-aligned PWM under light-load condition. $v_{gs'i'}$: Gate–source voltage of the $'i'$th switch; v_{Lr}: Voltage across L_r; t_d: Dead time.

resonant tank parameters. A prototype bidirectional converter operating at 40−50 V input voltage, 380 V output voltage, and 400 W output power is built and its expected performance is demonstrated.

This article is organized as follows. The circuit operations of the proposed converter are described in Section II, and its steady-state analysis is given in Section III to derive the nominal duty ratio of the secondary side, the threshold load level, and the desired amount of the phase shift. The controller design is presented in Section IV, and the experimental results and the discussions are drawn in Section V. The conclusion is given in Section VI.

II. Circuit Operation

Fig. 1 shows the circuit diagram of the proposed bidirectional resonant converter. V_L is the low voltage source and V_H is the

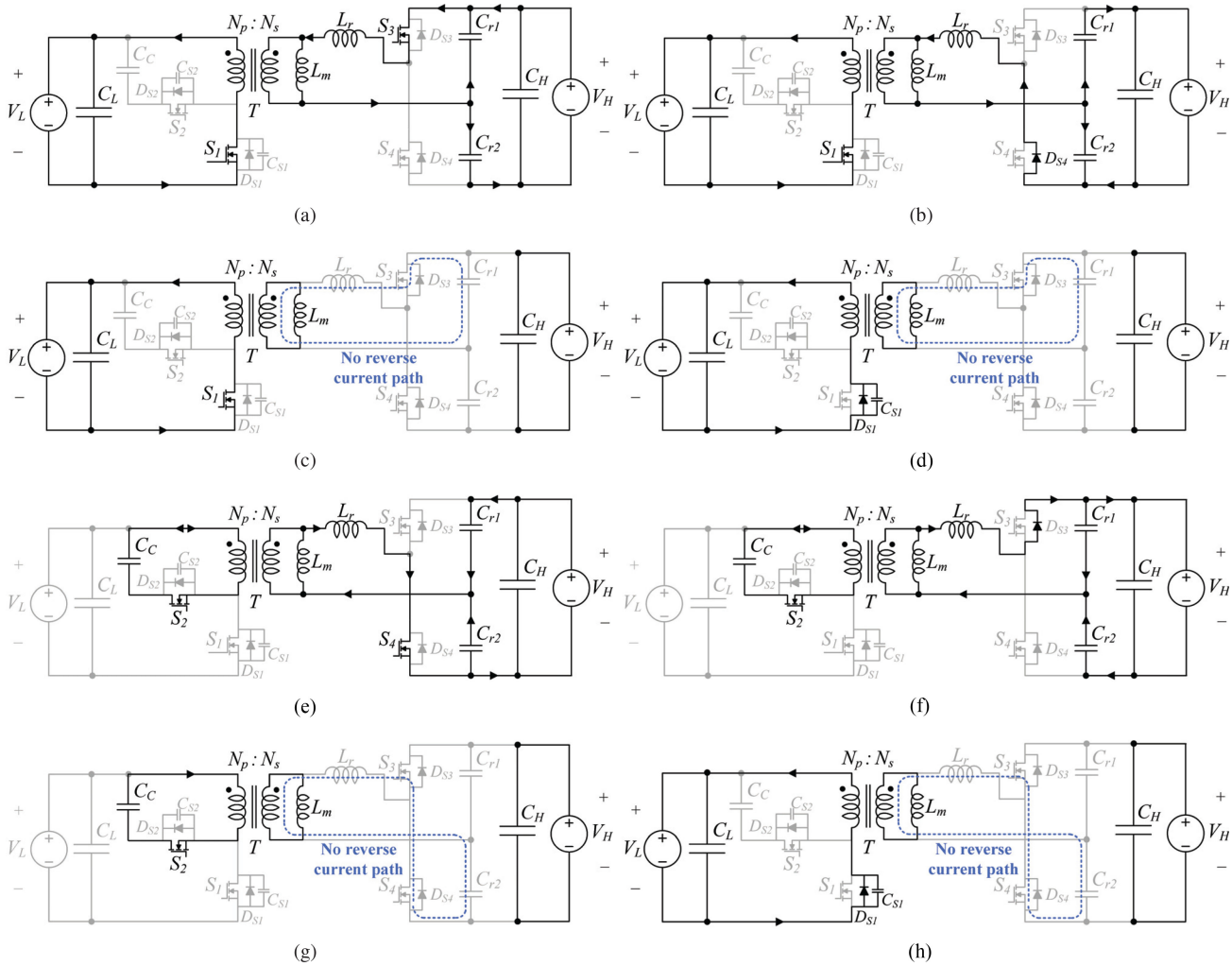

Fig. 3. Equivalent circuits of the proposed converter for backward operation with left-aligned PWM signals under light-load condition. (a) Mode 1^L. (b) Mode 2^L. (c) Mode 3^L. (d) Mode 4^L. (e) Mode 5^L. (f) Mode 6^L. (g) Mode 7^L. (h) Mode 8^L.

high voltage output when the converter is used for forward operation. On the other hand, V_H is the high voltage source and V_L is the low voltage output when it is used for backward operation. The transformer T has turns ratio of $n = N_s/N_p$, where N_p is the number of primary winding turns and N_s is the number of secondary winding turns. The primary side of the power transformer T is equipped with two switches S_1, S_2 and a clamp capacitor C_c. The secondary side of T is composed of a resonant half-bridge circuit that uses two switches S_3, S_4, two resonant capacitors C_{r1}, C_{r2}, and a resonant inductor L_r.

The primary switches S_1, S_2 operate in a complementary way with constant duty ratio $D_{\text{pri}} = 0.5$. Given the switching period T_s, the switches are operated as follows. For forward operation, S_4 is turned ON during the first segment $D_{\text{sec}}T_s$ of the first half of T_s, whereas S_3 is turned ON during the first segment $D_{\text{sec}}T_s$ of the next half of T_s. For backward operation, S_3 is turned ON during the first segment $D_{\text{sec}}T_s$ of the first half of T_s, whereas S_4 is turned ON during the first segment $D_{\text{sec}}T_s$ of the next half of T_s. In both power transfer operations, the proposed converter fixes the duty cycle D_{pri} of the primary-side switches at 0.5 and controls D_{sec}. But, in the case of backward operation, the instantaneous reactive power may occur and we attempt to remove it by adjusting the phase of the PWM signals. Note that this design technique differs from the conventional dual series resonant converter [23] that transfers power in a unidirectional way and is controlled by adjusting D_{pri} only.

To derive the circuit equations corresponding to different operation modes in the steady state, we make the following four assumptions.

1) Switches S_1, S_2, S_3, and S_4 in the proposed converter are ideal except for their reverse body diodes D_{S1}, D_{S2}, D_{S3}, and D_{S4} and output capacitances C_{S1} and C_{S2}.
2) The clamp capacitor C_c, the input capacitor C_L, and the output capacitor C_H are sufficiently large that the clamp capacitor voltage V_C, the low-side voltage V_L, and the high-side voltage V_H have no ripple.
3) T is composed of an ideal transformer with a magnetizing inductance L_m and leakage inductance.
4) The resonant capacitors C_{r1} and C_{r2} are identical, with capacitances $C_{r1} = C_{r2}$.

Here, we connected the external leakage inductor in series with secondary-side leakage inductance of the transformer to make a required resonant inductance L_r. We also define $C_r = C_{r1} + C_{r2}$ and assume that $C_{S1} = C_{S2}$.

During switching period T_s, the operation of the proposed converter can be divided into eight modes according to the switching operations of S_1–S_4. During the first half-switching period, detailed waveforms in the circuit are analyzed in the following sections. During the second half-switching period, waveforms are similar to the modes in the first half-switching period. Four modes in the first half-switching period are almost similar to four modes in the second half-switching period. The difference lies in that the clamp capacitor voltage instead of the low-side voltage is applied to the primary-side voltage of the transformer, thereby that we omitted analysis of four modes in the second half-switching period.

A. Backward Mode Operation With Left-Aligned PWM Signals Under Light-Load Condition

Since the circuit operation for forward power transfer is given in [20], we present only backward power transfer in this section. In the backward direction, the circuit operates in a resonant buck mode and transfers energy from V_H to V_L. The switching mechanism in this case is the same as that in the forward power transfer except that the switching sequence of S_3 and S_4 are reversed. S_3 is turned ON during the first half of the period, while S_4 is turned ON during the next half of the period. As shown in Fig. 2, i_{Lr} in the backward operation suffers no reverse current under light-load conditions.

Mode 1^L [t_0^L, t_1^L]: At time t_0^L, S_1 and S_3 get turned ON. S_1 is turned ON with ZVS because D_{S1} was already ON before mode 1^L starts. i_{Lr} begins to flow, and v_{Cr1} begins to decrease from its maximum value. During this interval, V_L, L_r, and C_r form an equivalent closed circuit that drives $|i_{Lr}|$ to increase following the uphill side of the sinusoidal waveform. The state equation corresponding to this equivalent circuit can be written as follows:

$$L_r \frac{di_{Lr}(t)}{dt} = nV_L - v_{Cr1}(t) \tag{1}$$

$$i_{Lr}(t) = C_r \frac{dv_{Cr1}(t)}{dt} \tag{2}$$

with $i_{Lr}(t_0^L) = 0$ and $v_{Cr1}(t_0^L) = \frac{V_H}{2} + \Delta V_{Cr}$ where ΔV_{Cr} is the voltage ripple across C_{r1} as shown in Fig. 2. Solving (1) and (2) yields the following:

$$i_{Lr}(t) = -\frac{r_b}{Z_r} \sin\left[\omega_r (t - t_0^L)\right] \tag{3}$$

$$v_{Cr1}(t) = nV_L + r_b \cos\left[\omega_r (t - t_0^L)\right] \tag{4}$$

where $\omega_r = 1/\sqrt{L_r C_r}$, $Z_r = \sqrt{L_r/C_r}$, and $r_b = \frac{V_H}{2} + \Delta V_{Cr} - nV_L$.

Mode 2^L [t_1^L, t_2^L]: At time t_1^L, S_3 gets turned OFF. The current on the secondary side then flows through D_{S4}. During this interval, $|i_{Lr}|$ goes to zero following the downhill side of sinusoidal waveform. The state equation corresponding to this equivalent circuit can be written as follows:

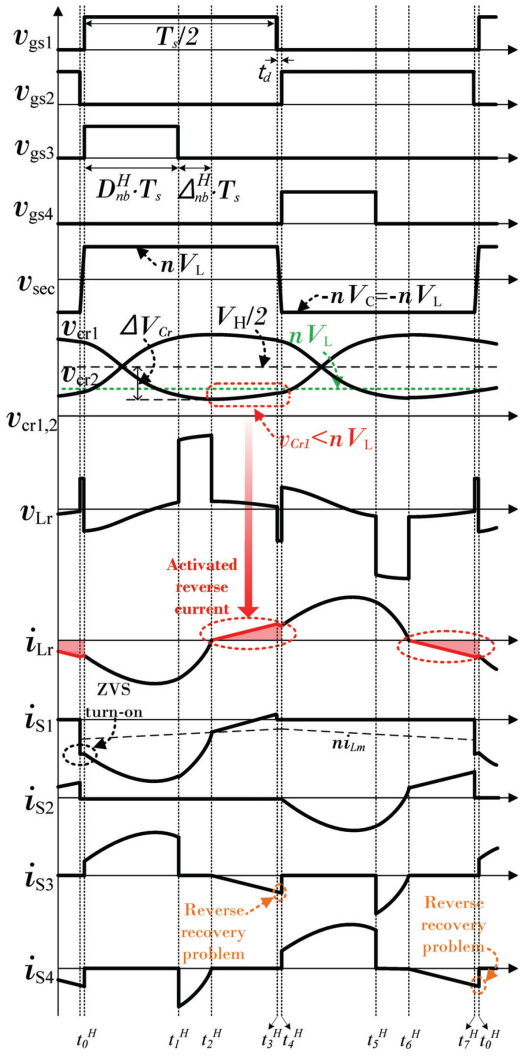

Fig. 4. Voltage, current, and switch waveforms for backward operation with left-aligned PWM under heavy-load condition. Red shaded area denotes the reverse current.

$$L_r \frac{di_{Lr}(t)}{dt} = nV_L + V_H - v_{Cr1}(t) \tag{5}$$

$$i_{Lr}(t) = C_r \frac{dv_{Cr1}(t)}{dt}. \tag{6}$$

Solving (5) and (6) with boundary conditions of (3) and (4) at t_1^L yields the following:

$$i_{Lr}(t) = \frac{1}{Z_r} \begin{pmatrix} -r_b \sin\left[\omega_r (t - t_0^L)\right] \\ +V_H \sin\left[\omega_r (t - t_1^L)\right] \end{pmatrix} \tag{7}$$

$$v_{Cr1}(t) = nV_L + V_H + r_b \cos\left[\omega_r (t - t_0^L)\right] - V_H \cos\left[\omega_r (t - t_1^L)\right]. \tag{8}$$

Mode 3^L [t_2^L, t_3^L]: At t_2^L, D_{S4} is turned OFF with ZCS. The drain–source voltage across S_3 is $v_{Cr1}(t) - nV_L$, which is positive as in Fig. 2. D_{S3} is reverse biased and the reverse current does not flow through D_{S3}. Therefore, the reverse current path is inactive as in Fig. 3(c).

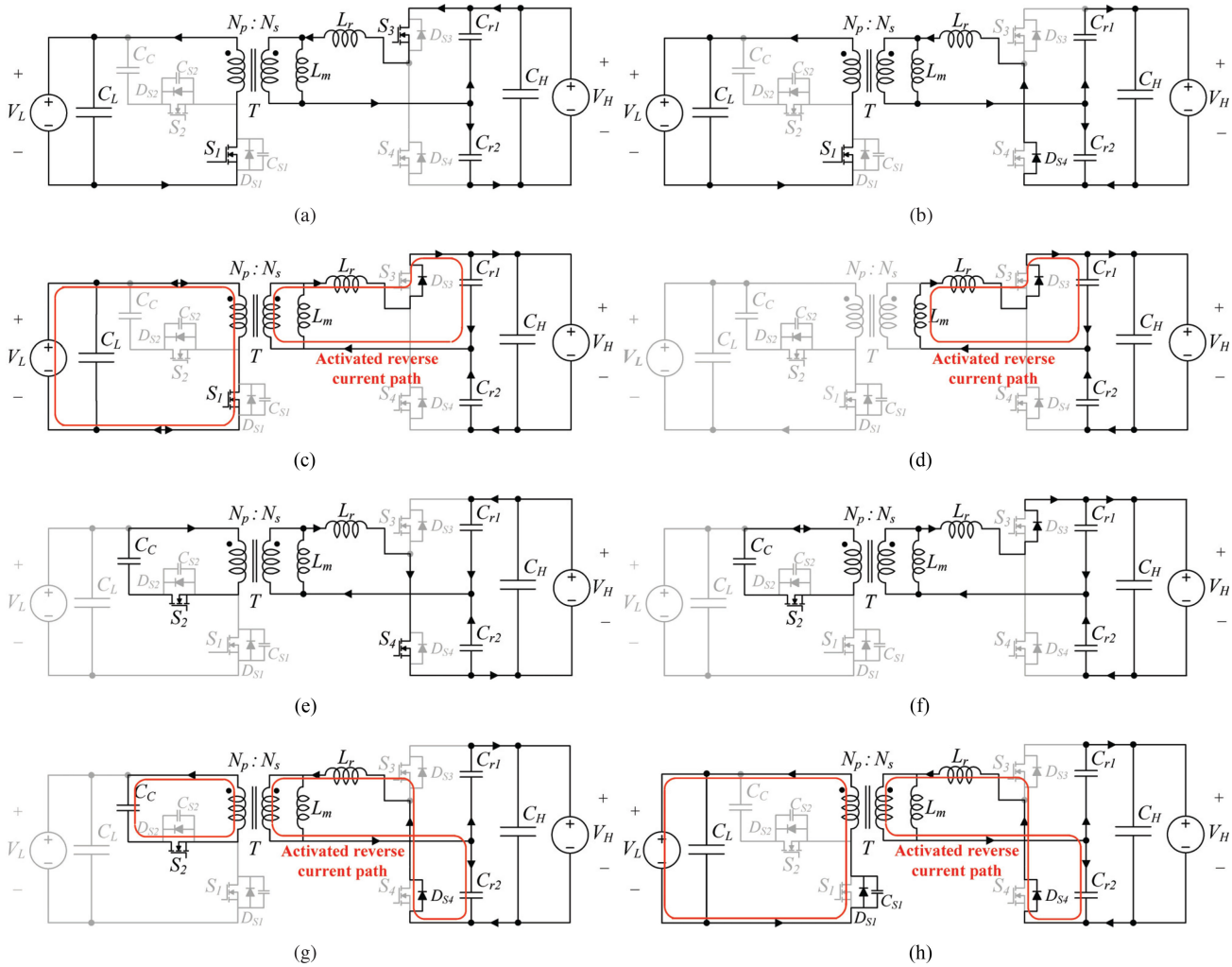

Fig. 5. Equivalent circuits of the proposed converter for backward operation with left-aligned PWM signals under heavy-load condition. (a) Mode 1^H. (b) Mode 2^H. (c) Mode 3^H. (d) Mode 4^H. (e) Mode 5^H. (f) Mode 6^H. (g) Mode 7^H. (h) Mode 8^H.

Mode 4^L [t_3^L, t_4^L]: At t_3^L, S_1 is turned OFF and enters the dead-time zone. During this time, D_{S3} is still reverse biased and the reverse current does not flow through D_{S3}. Therefore, the reverse current path is inactive as in Fig. 3(d).

B. Backward Mode Operation With Left-Aligned PWM Signals Under Heavy-Load Conditions

As the output load increases, it may reach the threshold level, above which the converter circuit may suffer from the reverse current, as in Fig. 4. The reverse current flows during $[t_2^H, t_3^H]$ and $[t_5^H, t_6^H]$, which generates the instantaneous reactive power and significantly increases the conduction loss of the converter. In this case, C_r suffers from large fluctuation during the resonant period, which in turn changes the polarity of v_{Lr} and makes the reverse current flow through D_{S3} or D_{S4}. Consequently, we can define the light load as the one below this threshold level and the heavy load as the one above it.

Mode 1^H [t_0^H, t_1^H]: At time t_0^H, S_1 and S_3 get turned ON. S_1 is turned ON with ZVS because D_{S1} was already ON before mode 1^H starts. i_{Lr} begins to flow, and v_{Cr1} begins to decrease. During this interval, V_L, L_r, and C_r form an equivalent closed circuit that drives $|i_{Lr}|$ to increase following the uphill side of the sinusoidal waveform. The state equation for L_r and C_r is given as follows:

$$L_r \frac{di_{Lr}(t)}{dt} = nV_L - v_{Cr1}(t) \tag{9}$$

$$i_{Lr}(t) = C_r \frac{dv_{Cr1}(t)}{dt}. \tag{10}$$

Solving (9) and (10) with $i_{Lr}(t_0^H) = -i_{Lr}(t_3^H)$ and $v_{Cr1}(t_0^H) = V_H - v_{Cr1}(t_3^H)$ yields the following:

$$i_{Lr}(t) = -\frac{r_3}{Z_r}\sin\left[\omega_r(t - t_0^H + t_3^H - t_2^H)\right] - \frac{V_H - 2nV_L}{Z_r}\sin\left[\omega_r(t - t_0^H)\right] \tag{11}$$

$$v_{Cr1}(t) = nV_L + r_3\cos\left[\omega_r(t - t_0^H + t_3^H - t_2^H)\right] + (V_H - 2nV_L)\cos\left[\omega_r(t - t_0^H)\right] \tag{12}$$

where $r_3 = -\frac{V_H}{2} + \Delta V_{Cr} + nV_L$.

Mode 2^H [t_1^H, t_2^H]: At time t_1^H, S_3 gets turned OFF. The current on the secondary side then flows through D_{S4}. During this interval, $|i_{Lr}|$ goes to zero following the downhill side of the sinusoidal waveform. The state equation in this mode is the same as (5) and (6)

$$L_r \frac{di_{Lr}(t)}{dt} = nV_L + V_H - v_{Cr1}(t) \tag{13}$$

$$i_{Lr}(t) = C_r \frac{dv_{Cr1}(t)}{dt}. \tag{14}$$

Solving (13) and (14) with $i_{Lr}(t_2^H) = 0$ and $v_{Cr1}(t_2^H) = \frac{V_H}{2} - \Delta V_{Cr}$ yields the following:

$$i_{Lr}(t) = \frac{r_1}{Z_r} \sin\left[\omega_r (t - t_2^H)\right] \tag{15}$$

$$v_{Cr1}(t) = nV_L + V_H - r_1 \cos\left[\omega_r (t - t_2^H)\right] \tag{16}$$

where $r_1 = \frac{V_H}{2} + \Delta V_{Cr} + nV_L$. This mode ends when i_{Lr} becomes zero.

Mode 3^H [t_2^H, t_3^H]: At t_2^H, D_{S4} is turned OFF with ZCS and D_{S3} is turned ON. The drain–source voltage across S_3 is $v_{Cr1}(t) - nV_L$, which is negative, as in Fig. 4. D_{S3} is forward biased and the reverse current flows through D_{S3}. Therefore, the reverse current path becomes active, as in Fig. 5(c). The state equation for this mode is given by

$$L_r \frac{di_{Lr}(t)}{dt} = nV_L - v_{Cr1}(t) \tag{17}$$

$$i_{Lr}(t) = C_r \frac{dv_{Cr1}(t)}{dt}. \tag{18}$$

Solving (17) and (18) with $i_{Lr}(t_2^H) = 0$ and $v_{Cr1}(t_2^H) = \frac{V_H}{2} - \Delta V_{Cr}$ yields the following:

$$i_{Lr}(t) = \frac{r_3}{Z_r} \sin\left[\omega_r (t - t_2^H)\right] \tag{19}$$

$$v_{Cr1}(t) = nV_L - r_3 \cos\left[\omega_r (t - t_2^H)\right]. \tag{20}$$

Mode 4^H [t_3^H, t_4^H]: At t_3^H, S_1 is turned OFF and enters the dead-time zone. During this time, D_{S3} is still forward biased and the reverse current flows through D_{S3}. Therefore, the reverse current path is still active, as in Fig. 5(d).

C. Backward Mode Operation With Phase Adjusted PWM Signals Under Heavy-Load Condition

But by using the PWM signals with the correct phase shift, we can verify that the reverse current and the instantaneous reactive power disappear, as shown in Fig. 6. The required amount of time duration to remove this reverse current is $t_3^L - t_2^L$ in Fig. 2 which is the same as $t_1 - t_0$ in Fig. 6.

Mode 1 [t_0, t_1]: At time t_1, S_1 gets turned ON with ZVS because D_{S1} was already ON before mode 1 starts. The drain–source voltage across S_3 is $v_{Cr1}(t) - nV_L$, which is positive, as in Fig. 6. D_{S3} is reverse biased and the reverse current does not flow through D_{S3}. Therefore, the reverse current path is inactive, as in Fig. 7(a).

Mode 2 [t_1, t_2]: At time t_1, S_3 gets turned ON. i_{Lr} begins to flow, and v_{Cr1} begins to decrease from its maximum value.

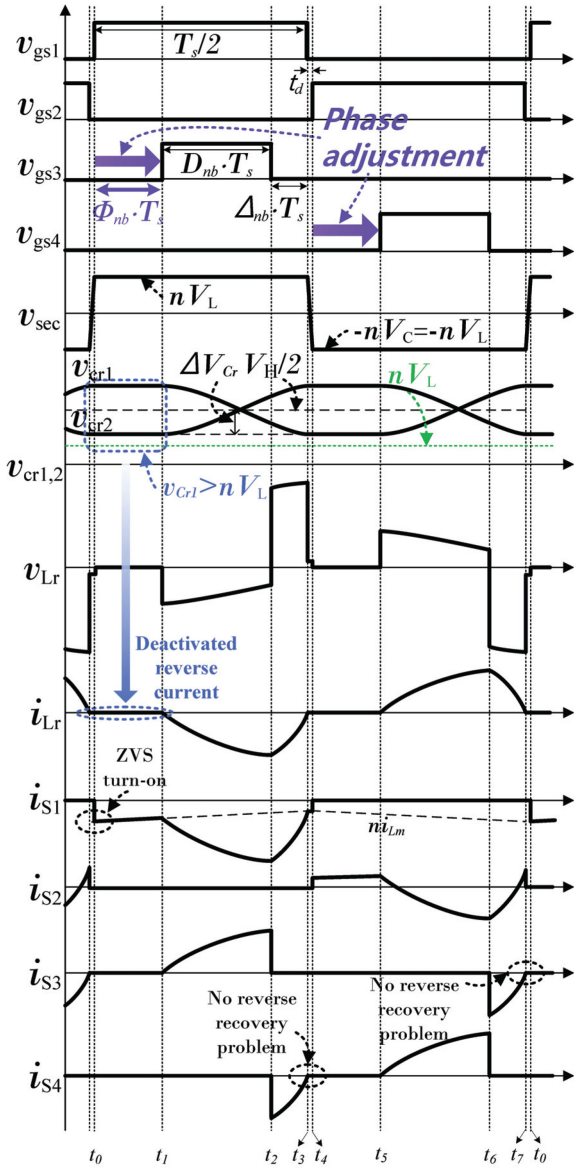

Fig. 6. Voltage, current and switch waveforms for backward operation with phase adjusted PWM under heavy-load condition.

During this interval, V_L, L_r, and C_r form an equivalent closed circuit, and $|i_{Lr}|$ increases following the uphill side of the sinusoidal waveform. The state equation corresponding to this equivalent circuit can be written as follows:

$$L_r \frac{di_{Lr}(t)}{dt} = nV_L - v_{Cr1}(t) \tag{21}$$

$$i_{Lr}(t) = C_r \frac{dv_{Cr1}(t)}{dt} \tag{22}$$

with $i_{Lr}(t_1) = 0$ and $v_{Cr1}(t_1) = \frac{V_H}{2} + \Delta V_{Cr}$, as shown in Fig. 6. Solving (21) and (22) yields the following:

$$i_{Lr}(t) = -\frac{r_b}{Z_r} \sin\left[\omega_r (t - t_1)\right] \tag{23}$$

$$v_{Cr1}(t) = nV_L + r_b \cos\left[\omega_r (t - t_1)\right]. \tag{24}$$

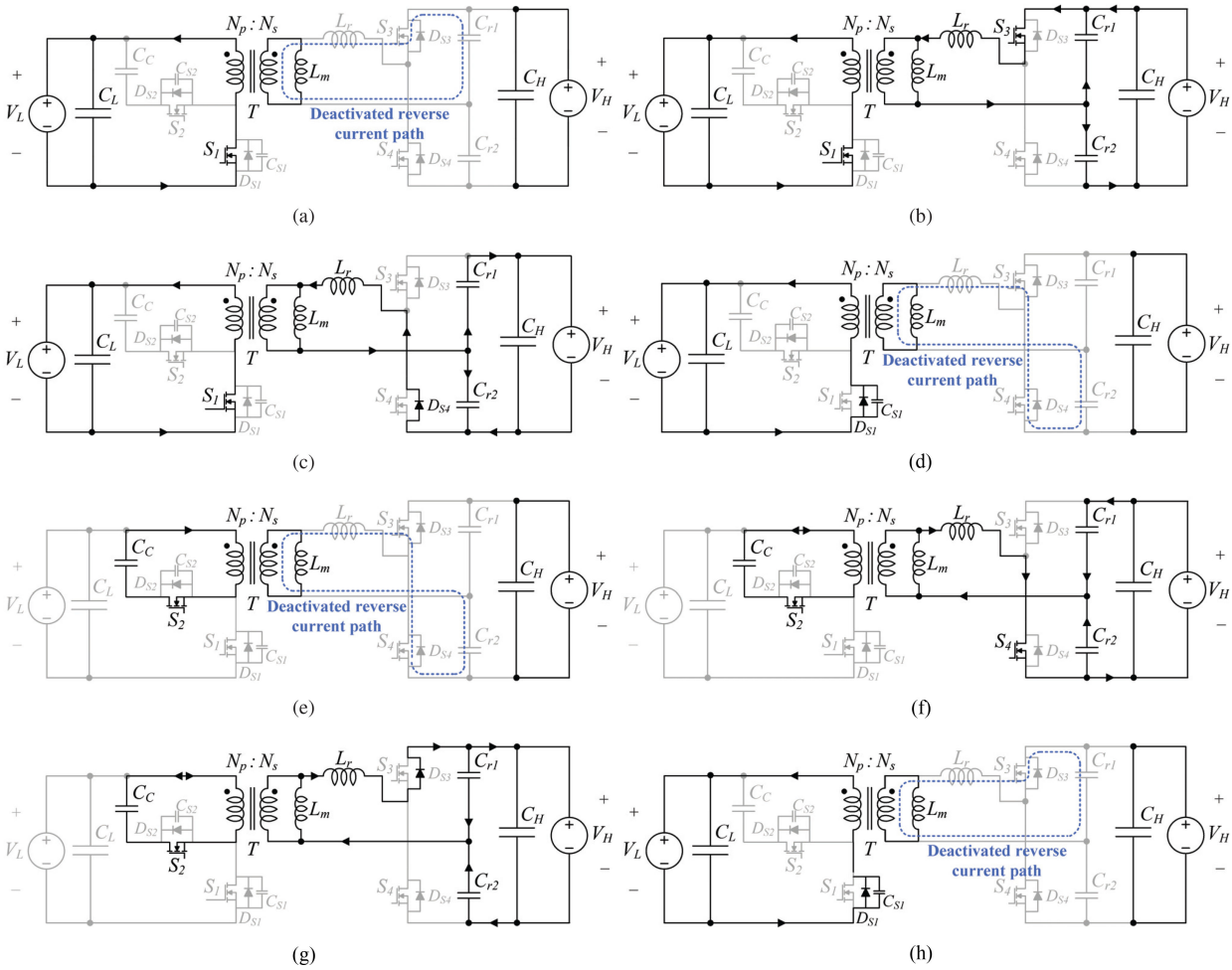

Fig. 7. Equivalent circuits of the proposed converter for backward operation with phase adjusted PWM under heavy-load condition. (a) Mode 1. (b) Mode 2. (c) Mode 3. (d) Mode 4. (e) Mode 5. (f) Mode 6. (g) Mode 7. (h) Mode 8.

Mode 3 [t_2, t_3]: At time t_2, S_3 gets turned OFF. The current on the secondary side then flows through D_{S4}. During this interval, $|i_{Lr}|$ goes to zero following the downhill side of the sinusoidal waveform. The state equation corresponding to this equivalent circuit can be written as follows:

$$L_r \frac{di_{Lr}(t)}{dt} = nV_L + V_H - v_{Cr1}(t) \tag{25}$$

$$i_{Lr}(t) = C_r \frac{dv_{Cr1}(t)}{dt}. \tag{26}$$

Solving (25) and (26) with $i_{Lr}(t_3) = 0$ and $v_{Cr1}(t_3) = \frac{V_H}{2} - \Delta V_{Cr}$ yields the following:

$$i_{Lr}(t) = \frac{1}{Z_r} \begin{pmatrix} -r_b \sin\left[\omega_r(t-t_1)\right] \\ +V_H \sin\left[\omega_r(t-t_2)\right] \end{pmatrix} \tag{27}$$

$$v_{Cr1}(t) = nV_L + V_H + r_b \cos\left[\omega_r(t-t_1)\right] - V_H \cos\left[\omega_r(t-t_2)\right]. \tag{28}$$

Mode 4 [t_3, t_4]: At time t_3, D_{S4} is turned OFF with ZCS. The drain–source voltage across S_4 is $v_{Cr2}(t) - nV_L$, which is positive, as in Fig. 6. D_{S4} is reverse biased and the reverse current does not flow through D_{S4}. Therefore, the reverse current path is inactive, as in Fig. 7(d).

III. Steady-State Analysis

When D_{pri} is set to 0.5, V_C becomes the same as V_L, and, consequently, V_{Cr1} and V_{Cr2} are equally balanced. With this setting, we first derive the nominal duty ratio D_{nb} of the secondary side in terms of backward voltage gain M_b, then derive the threshold level load P_{th}, above which the instantaneous reactive power appears, compute the required amount of phase shift to remove this instantaneous reactive power, and analyze the sensitivity of the required amount of phase with regard to resonant tank parameters.

A. Nominal Duty Ratio of the Secondary Side

In order to calculate the nominal duty ratio D_{nb} for backward operation, we first need to derive voltage ripple ΔV_{Cr} of $C_{r1,2}$.

First, we obtain the average output power P_o as follows:

$$P_o = \frac{V_L}{T_s}\int_{t_0}^{t_0+T_s/2} 2n\cdot|i_{Lr}(\tau)|d\tau = \frac{4nV_LC_r}{T_s}\Delta V_{Cr}. \quad (29)$$

Rearranging (29) yields the following:

$$\Delta V_{Cr} = \lambda_b n V_L, \quad (30)$$

where $\lambda_b = \frac{P_oT_s}{4n^2V_L^2C_r}$.

Using the facts that $i_{Lr}(t_3)=0$ and $v_{Cr1}(t_3)=\frac{V_H}{2}-\Delta V_{Cr}$ at $t=t_3$ in Fig. 6, we can arrange (27) and (28) as follows:

$$r_b\sin[\omega_r(t_3-t_1)] - V_H\sin[\omega_r(t_3-t_2)] = 0 \quad (31)$$

$$r_b\cos[\omega_r(t_3-t_1)] - V_H\cos[\omega_r(t_3-t_2)]$$
$$= \left(\frac{V_H}{2}-\Delta V_{Cr}\right) - nV_L - V_H = -r_f, \quad (32)$$

where $r_f = \frac{V_H}{2}+\Delta V_{Cr}+nV_L$.

Squaring both sides of (31) and (32) and adding the resulting equations yield the following:

$$r_f^2 = r_b^2 + V_H^2 - 2r_bV_H(\cos[\omega_r(t_3-t_1)]\cos[\omega_r(t_3-t_2)]$$
$$+\sin[\omega_r(t_3-t_1)]\sin[\omega_r(t_3-t_2)])$$
$$= r_b^2 + V_H^2 - 2r_bV_H\cos[\omega_r(t_2-t_1)]. \quad (33)$$

Since $t_2-t_1 = D_{nb}T_s$, rearranging (33) yields the following:

$$\cos[\omega_r(t_2-t_1)] = \cos(\omega_rD_{nb}T_s)$$
$$= \frac{r_b^2-r_f^2+V_H^2}{2r_bV_H} = \frac{-2nV_L(V_H+2\Delta V_{Cr})+V_H^2}{V_H(V_H+2\Delta V_{Cr}-2nV_L)}$$
$$= \frac{-2nV_L(V_H+2n\lambda_bV_L)+V_H^2}{V_H(V_H+2n\lambda_bV_L-2nV_L)} = \frac{1-M_b-\lambda_bM_b^2}{1-M_b+\lambda_bM_b} \quad (34)$$

where $M_b = \frac{2nV_L}{V_H}$ is the backward voltage gain. From (34), it follows that

$$D_{nb} = \frac{1}{\omega_rT_s}\cos^{-1}\left(\frac{1-M_b-\lambda_bM_b^2}{1-M_b+\lambda_bM_b}\right). \quad (35)$$

A three-dimensional graph of M_b with respect to P_o and D_{nb} is shown in Fig. 8. Rearranging (35), we can represent M_b in terms of D_{nb} as follows:

$$M_b = \frac{-(\lambda_b\cos(\omega_rD_{nb}T_s)-\cos(\omega_rD_{nb}T_s)+1) + \sqrt{\begin{array}{c}(\lambda_b\cos(\omega_rD_{nb}T_s)-\cos(\omega_rD_{nb}T_s)+1)^2\\ -4\lambda_b(\cos(\omega_rD_{nb}T_s)-1)\end{array}}}{2\lambda_b}. \quad (36)$$

B. Threshold Load

If the left-aligned PWM is used without any phase adjustment, the reverse current starts to appear when the voltage across the inductor v_{Lr} becomes positive at t_2^H, as shown in Fig. 4. This condition can be written as follows:

$$v_{Lr}(t_2^L) = nV_L - v_{Cr1}(t_2^L)$$

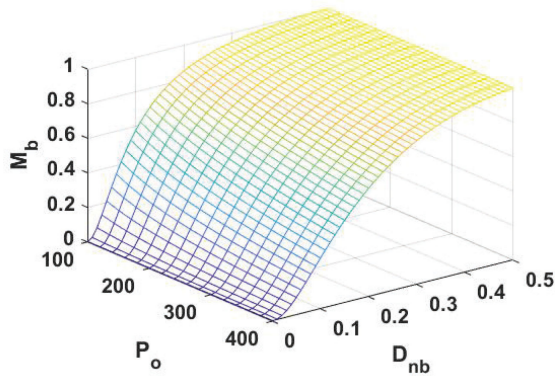

Fig. 8. Three-dimensional graph of M_b versus P_o and D_{nb}.

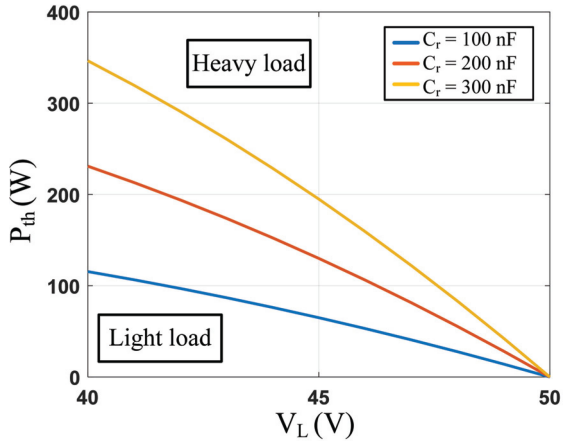

Fig. 9. Threshold load P_{th} versus V_L with $C_r = 100, 200$, and 300 nF. V_H is fixed at 380 V.

$$= nV_L - \left(\frac{V_H}{2}-\Delta V_{Cr}\right) > 0. \quad (37)$$

From (30) and (37), it follows that

$$P_o > \left(\frac{V_H}{2}-nV_L\right)\cdot\frac{4nV_LC_r}{T_s}. \quad (38)$$

Rearranging (38) results in

$$P_o > P_{th} = \left(\frac{1}{M_b}-1\right)\cdot\frac{4n^2V_L^2C_r}{T_s} \quad (39)$$

where P_{th} is the threshold load. A graph of P_{th} versus V_L with three different C_r values is shown in Fig. 9. If (39) holds, it is a heavy-load case and the instantaneous reactive power is bound to appear. In this case, we need to apply the right amount of phase shift to remove it. The desired amount of phase shift is in fact $t_3^L - t_2^L$, as shown in Fig. 2.

C. Required Amount of Phase Shift to Remove Instantaneous Reactive Power

Since the required amount of phase shift $t_3^L - t_2^L$ in Fig. 2 is the same as $t_1 - t_0$ in Fig. 6, we attempt to compute $t_1 - t_0$, as given in Fig. 6. Moving $V_H\sin[\omega_r(t_3-t_2)]$ and $V_H\cos[\omega_r(t_3-t_2)]$ terms to the right-hand side of (31) and

(32), squaring both sides of the resulting equations, and adding them yield

$$r_b^2 = V_H^2 + r_f^2 - 2r_f V_H \cos\left[\omega_r(t_3 - t_2)\right] \tag{40}$$

and rearranging (40) yields

$$\cos\left[\omega_r(t_3 - t_2)\right] = \cos\left(\omega_r \Delta_{nb} T_s\right) = \frac{r_f^2 - r_b^2 + V_H^2}{2r_f V_H} = \frac{1 + M_b + \lambda_b M_b^2}{1 + M_b + \lambda_b M_b}. \tag{41}$$

Δ_{nb} can then be derived as follows:

$$\Delta_{nb} = \frac{1}{\omega_r T_s} \cos^{-1}\left(\frac{1 + M_b + \lambda_b M_b^2}{1 + M_b + \lambda_b M_b}\right). \tag{42}$$

Since $(t_1 - t_0) = T_s/2 - (t_2 - t_1) - (t_3 - t_2) = T_s/2 - D_{nb} T_s - \Delta_{nb} T_s$ from Fig. 6, we can calculate from (35) and (42) that the desired amount of phase shift becomes

$$t_1 - t_0 = \frac{1}{2}T_s - \frac{1}{\omega_r}\cos^{-1}\left(\frac{1 - M_b - \lambda_b M_b^2}{1 - M_b + \lambda_b M_b}\right) - \frac{1}{\omega_r}\cos^{-1}\left(\frac{1 + M_b + \lambda_b M_b^2}{1 + M_b + \lambda_b M_b}\right). \tag{43}$$

D. Sensitivity Analysis

We analyzed sensitivity of the right amount of phase with regard to the resonant parameter variations. As the right amount of phase is $\phi_{nb} = \frac{1}{2} - D_{nb} - \Delta_{nb}$, the sensitivity of ϕ_{nb} with regard to L_r can be obtained as in [21], [22] as follows:

$$S_{\phi_{nb}}^{L_r} = \frac{L_r}{\phi_{nb}} \cdot \frac{d\phi_{nb}}{dL_r} = \frac{L_r}{\phi_{nb}} \cdot \frac{d}{dL_r}\left(\frac{1}{2} - D_{nb} - \Delta_{nb}\right) = -\frac{1}{2\phi_{nb}}\left(D_{nb} + \Delta_{nb}\right). \tag{44}$$

Denoting $\omega_r \phi_{nb} T_s = N_\phi$, the sensitivity of ϕ_{nb} with regard to C_r can also be obtained as follows:

$$S_{\phi_{nb}}^{C_r} = \frac{C_r}{\phi_{nb}} \cdot \frac{d\phi_{nb}}{dC_r} = \frac{C_r}{\phi_{nb}} \cdot \frac{d}{dC_r}\left(\frac{1}{2} - D_{nb} - \Delta_{nb}\right) = \frac{1}{N_\phi} \cdot \frac{1}{\sin(N_\phi)}\left(-\frac{N_\phi}{2} + \lambda_b M_b (M_b - 1)^2\right). \tag{45}$$

$S_{\phi_{nb}}^{L_r}$ and $S_{\phi_{nb}}^{C_r}$ with respect to normalized output power variation are described in Fig. 10. As the power is shifted to a large value, the sensitivity of ϕ_{nb} with regard to L_r becomes much higher than that with regard to C_r.

IV. Controller Design

In order to build a bidirectional converter, we implemented a bidirectional control strategy as given in Fig. 11. The overall controller consists of a current control part that calculates the duty ratio D_{sec} for both operations, the phase calculation part that calculates the right amount of phase ϕ_{nb} for backward operation, and a PWM generator incorporating D_{sec} and ϕ_{nb}. U_c signifies the power flow direction. When the power flows in forward, U_c is set to be zero. In backward operation, $U_c = 1$.

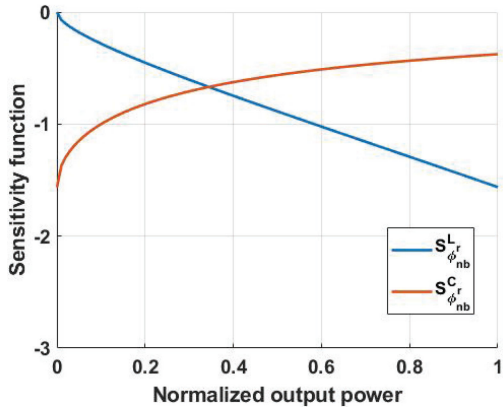

Fig. 10. Sensitivity functions $S_{\phi_{nb}}^{L_r}$ and $S_{\phi_{nb}}^{C_r}$ with regard to normalized output power variation.

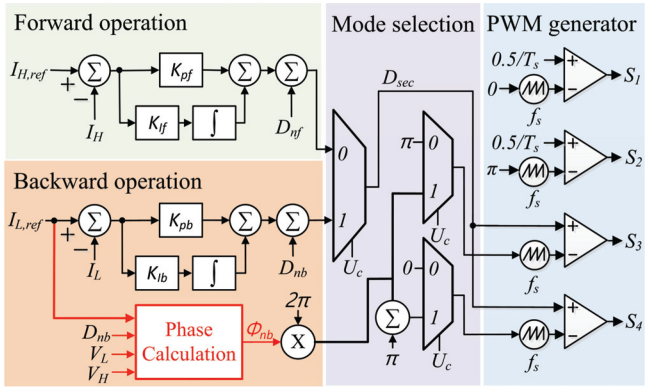

Fig. 11. Configuration of the proposed control scheme. $I_{H,\text{ref}}$ is the high-voltage side reference current. $I_{L,\text{ref}}$ is the low-voltage side reference current. K_{pf} and K_{if} are the proportional and integral control gains in the forward direction, respectively; K_{pb} and K_{ib} are the proportional and integral control gains in the backward direction, respectively. U_c indicates the power flow direction.

In the forward power transfer, the current controller first determines the high-voltage side current error first by subtracting I_H from $I_{H,ref}$. It is then supplied as an input to the proportional-integral (PI) current controller. The controller output is then added with the nominal duty D_{nf} to calculate the duty ratio D_{sec}, which is then used to control the secondary-side switches. D_{nf} is the feed-forward control input and can be given as follows:

$$D_{nf} = \frac{1}{\omega_r T_s}\cos^{-1}\left(\frac{1 + M_f + \lambda_f M_f}{1 + M_f + \lambda_f M_f^2}\right) \tag{46}$$

where $M_f = \frac{V_H}{2nV_L}$ is the forward voltage gain and $\lambda_f = \frac{4P_o T_s}{V_H^2 C_r}$.

In the backward power transfer, the current controller first determines the low-voltage side current error first by subtracting I_L from $I_{L,\text{ref}}$. The error is then supplied as an input to the PI controller. The controller output is then added with nominal duty D_{nb}, which is given as follows:

$$D_{nb} = \frac{1}{\omega_r T_s}\cos^{-1}\left(\frac{1 - M_b - \lambda_b M_b^2}{1 - M_b + \lambda_b M_b}\right). \tag{47}$$

TABLE I
PARAMETERS AND COMPONENTS OF THE PROTOTYPE CONVERTER

Parameters	Symbols	Values
Low-side voltage range	V_L	40 - 50 V
Nominal low-side voltage	V_{L_nom}	45 V
High-side voltage	V_H	380 V
Output power	P_o	400 W
Switching frequency	f_s	50 kHz
Resonant frequency	f_r	45.80 kHz
Transformer turn ratio	N_p:N_s	10:38
Magnetizing inductance	L_m	1.127 mH
Resonant inductance	L_r	60.38 μH
Resonant capacitance	C_{r1}, C_{r2}	100 nF
Low-side capacitance	C_L	560 μF
Clamp capacitance	C_c	10 μF
High-side capacitance	C_H	20 μF
Components	**Symbols**	**Part numbers**
Primary-side switches	S_1, S_2	IPP051N15N5
Secondary-side switches	S_3, S_4	UJC06505K
Transformer core	T	PQ4040

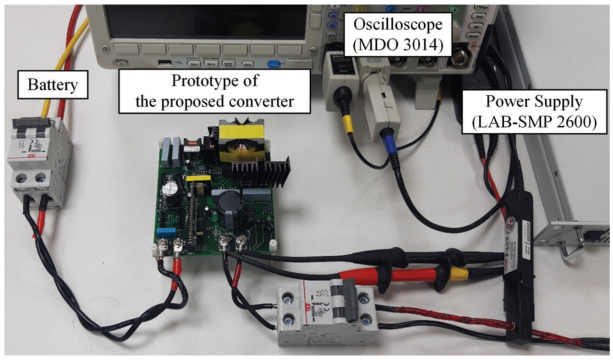

Fig. 12. Experimental setup of the proposed converter system.

Implementing the appropriately designed PI controller, we can expect that $D_{\text{sec}} \cong D_{nb}$ in the steady state. Also, the amount of phase shift required to remove the instantaneous reactive power is given in the previous section and is rewritten here as follows:

$$\begin{aligned}\phi_{nb} &= (t_1 - t_0)/T_s \\ &= \frac{1}{2} - \frac{1}{\omega_r T_s}\cos^{-1}\left(\frac{1 - M_b - \lambda_b M_b^2}{1 - M_b + \lambda_b M_b}\right) \\ &\quad - \frac{1}{\omega_r T_s}\cos^{-1}\left(\frac{1 + M_b + \lambda_b M_b^2}{1 + M_b + \lambda_b M_b}\right). \end{aligned} \tag{48}$$

V. EXPERIMENTAL RESULTS AND DISCUSSIONS

To evaluate the performance of the proposed converter, we conducted experimental tests using the 400-W prototype converter (Table I and Fig. 12) with low-side voltage $V_L = 40$–50 V, high-side voltage $V_H = 380$ V, and rated output power $P_o = 400$ W. The digital control algorithm is implemented using a TMS320F28069 microcontroller. The resonant capacitor and resonant inductor have been selected as $C_{r1} = C_{r2} = 100$ nF and $L_r = 60.38$ μH to guarantee ZCS resonance at S_3, S_4. We have selected $C_r = C_{r1} + C_{r2} = 200$ nF to reduce the reverse current effect in heavy load and the switching loss arising from the peak value of i_{Lr}, which is proportional to C_r. For PI gains of the current control algorithm, we set $K_{pf} = K_{pb} = 0.00047$ and $K_{if} = K_{ib} = 0.0013$.

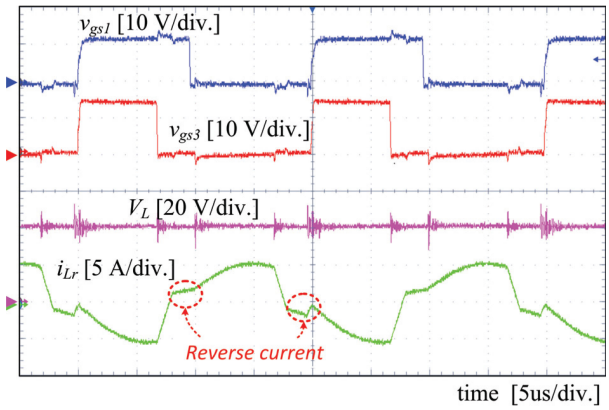

(a)

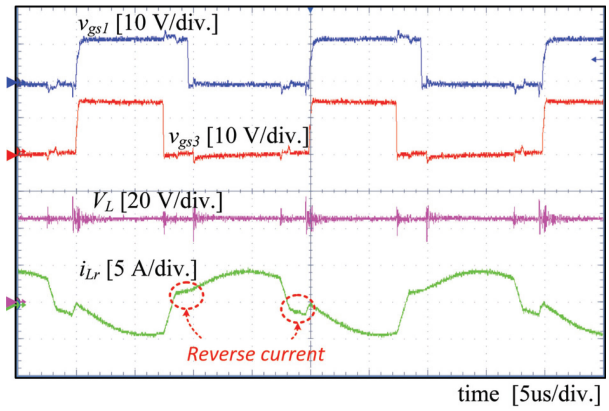

(b)

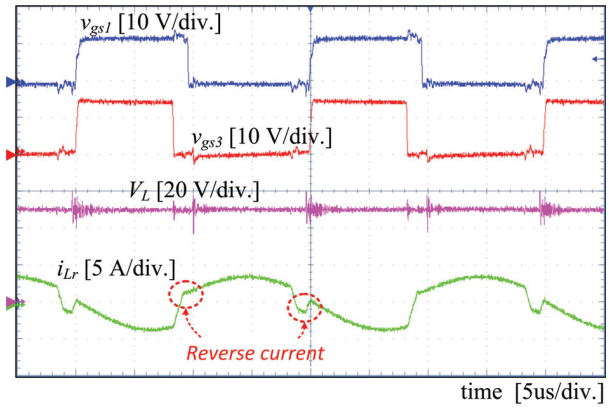

(c)

Fig. 13. Experimental waveforms of v_{gs1}, v_{gs3}, V_L, and i_{Lr} with $V_H = 380$ V and $P_o = 400$ W. (a) $V_L = 40$ V, $\phi_{nb} = 0$, $D_{\text{sec}} = 0.3$, and $P_{th} = 231$ W. (b) $V_L = 45$ V, $\phi_{nb} = 0$, $D_{\text{sec}} = 0.35$, and $P_{th} = 130$ W. (c) $V_L = 50$ V, $\phi_{nb} = 0$, $D_{\text{sec}} = 0.45$, and $P_{th} = 0$ W.

The v_{gs1}, v_{gs3}, V_L, and i_{Lr} waveforms in Fig. 13 show that the reverse current occurs and increases linearly when the left-aligned PWM is used without any phase adjustment. In the first half-switching period, the reverse current part of i_{Lr} does

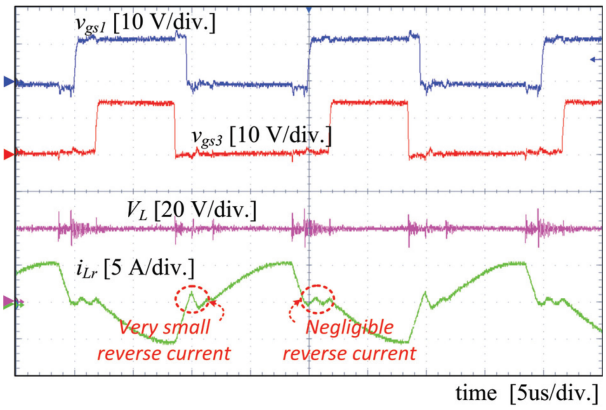

(a)

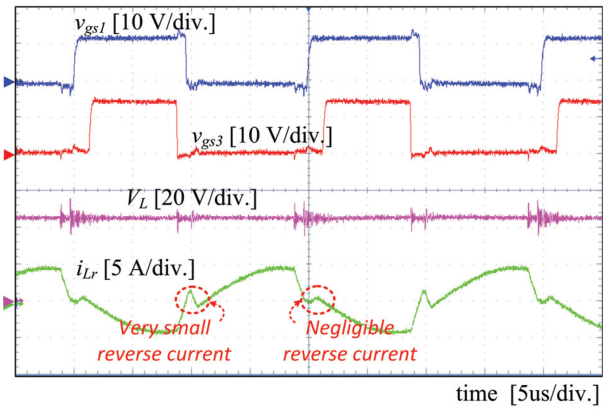

(b)

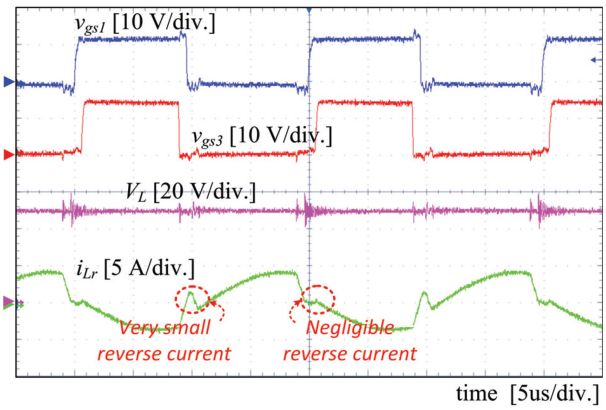

(c)

Fig. 14. Experimental waveforms of v_{gs1}, v_{gs3}, V_L, and i_{Lr} with $V_H = 380$ V and $P_o = 400$ W. (a) $V_L = 40$ V, $\phi_{nb} = 0.15$, $D_{\text{sec}} = 0.3$, and $P_{th} = 231$ W. (b) $V_L = 45$ V, $\phi_{nb} = 0.12$, $D_{\text{sec}} = 0.35$, and $P_{th} = 130$ W. (c) $V_L = 50$ V, $\phi_{nb} = 0.04$, $D_{\text{sec}} = 0.45$, and $P_{th} = 0$ W.

not go to zero and is similar to that in Fig. 4 because the current loop is formed through the body diode of S_2. But the reverse current part of i_{Lr} in Fig. 13 temporarily goes to zero in the second half-switching period because there exists a small dead time between S_2 and S_1. The v_{gs1}, v_{gs3}, V_L, and i_{Lr} waveforms in Fig. 14 show that the reverse current parts of i_{Lr} have been removed when the desired amount of phase shift has been applied to the PWM signals. If the adjusted phase shift is less than the

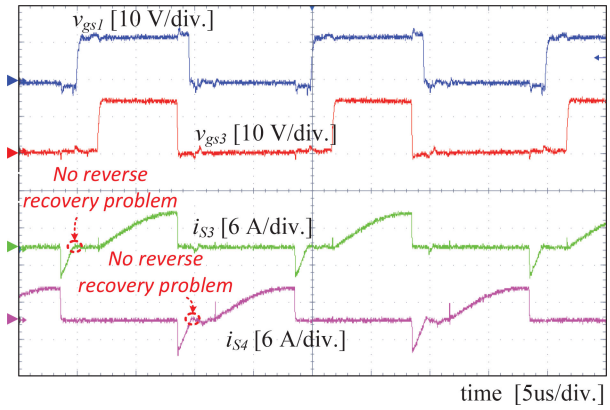

Fig. 15. Experimental waveforms of v_{gs1}, v_{gs3}, i_{S3}, and i_{S4} with $\phi_{nb} = 0.15$, $D_{\text{sec}} = 0.3$, $V_L = 40$ V, $V_H = 380$ V, $P_{th} = 231$ W, and $P_o = 400$ W.

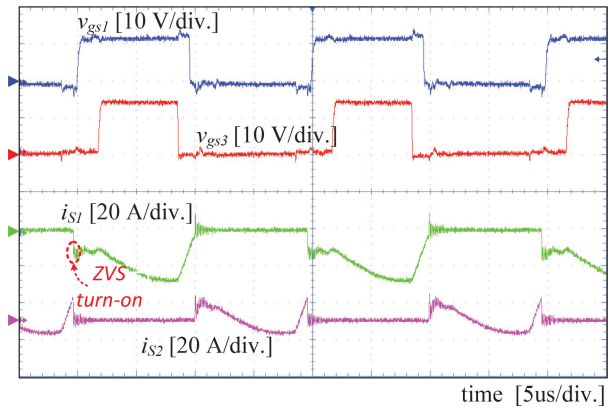

Fig. 16. Experimental waveforms of v_{gs1}, v_{gs3}, i_{S1}, and i_{S2} with $\phi_{nb} = 0.15$, $D_{\text{sec}} = 0.3$, $V_L = 40$ V, $V_H = 380$ V, $P_{th} = 231$ W, and $P_o = 400$ W.

desired one, the instantaneous reactive power may be decreased but cannot be removed. On the other hand, if the adjusted phase shift is more than the desired one, the instantaneous reactive power appears again. Thus, applying the right amount of phase shift is important to get rid of the instantaneous reactive power completely. When the secondary switch gets turned ON, L_r gets charged and i_{Lr} increases following the sinusoidal waveform. When the secondary switch gets turned OFF, L_r gets discharged and i_{Lr} decreases almost linearly. The resonance disappears when $i_{Lr} = 0$. In the proposed circuit, L_m is set to be large enough, and so the magnetizing inductor current is almost constant. It disconnects the primary-side voltage source from the resonant tank during the dead time between S_1 and S_2. Then, a very small reverse current flows due to the resonance between the parasitic capacitance of the secondary switches, the magnetizing inductance, and the resonant inductance. And the v_{gs1}, v_{gs3}, i_{S3}, and i_{S4} waveforms in Fig. 15 show that the current flows through S_3 and S_4 when the secondary switch gets turned ON. When the secondary switch gets turned OFF, the current begins to flow through D_{S3} and D_{S4}, and they get turned OFF at zero current, and so the reverse-recovery problem never occurs. The v_{gs1}, v_{gs3}, i_{S1}, and i_{S2} waveforms in Fig. 16 show that i_{S1} becomes negative when the clamp switch gets turned

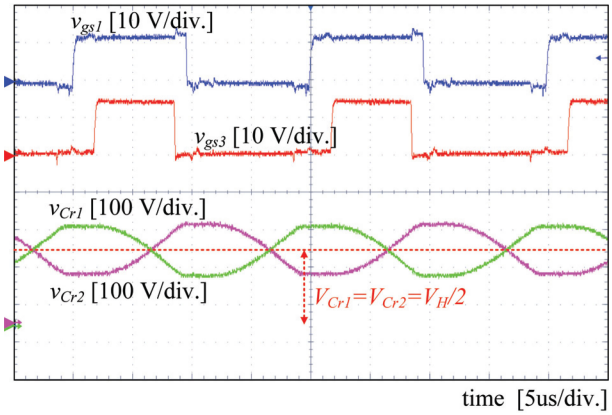

Fig. 17. Experimental waveforms of v_{gs1}, v_{gs3}, v_{Cr1}, and v_{Cr2} with $\phi_{nb} = 0.15$, $D_{\text{sec}} = 0.3$, $V_L = 40$ V, $V_H = 380$ V, $P_{th} = 231$ W, and $P_o = 400$ W.

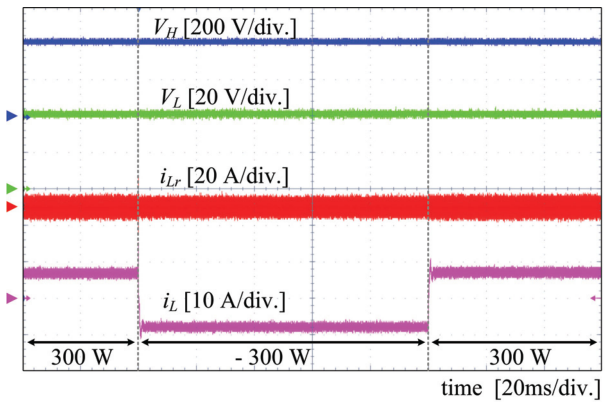

Fig. 18. Experimental waveforms of V_H, V_L, i_{Lr}, and i_L when power flow direction changes with $V_L = 40$ V and $V_H = 380$ V.

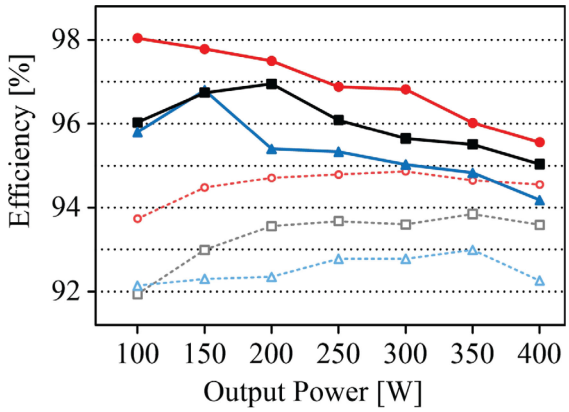

Fig. 19. Measured power conversion efficiency. Solid red line: $V_L = 50$ V with phase adjustment. Solid black line: $V_L = 45$ V with phase adjustment. Solid blue line: $V_L = 40$ V with phase adjustment. Dotted red line: $V_L = 50$ V without phase adjustment. Dotted black line: $V_L = 45$ V without phase adjustment. Dotted blue line: $V_L = 40$ V without phase adjustment.

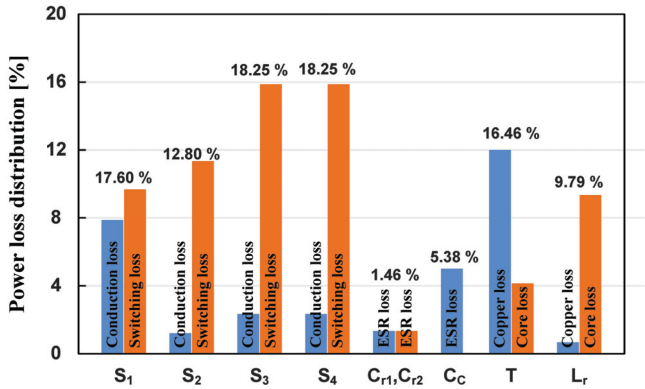

Fig. 20. Power loss distribution in the proposed converter operating in backward direction at full load.

OFF, achieving ZVS at the primary switch. The v_{gs1}, v_{gs3}, v_{Cr1}, and v_{Cr2} waveforms in Fig. 17 show voltage balance of v_{Cr1} and v_{Cr2} because D_{pri} is set to 0.5. In order to show the dynamic performance of the proposed converter, we changed the power flow from the forward direction to the backward direction and vice versa (Fig. 18). The primary current tracks the reference primary current well during power from forward to backward and vice versa.

The power conversion efficiency of the proposed converter operating in backward direction was measured using a Yokogawa WT330 digital power meter at 40, 45, and 50 V and with/without phase adjustment (Fig. 19). The converter operating in the backward direction achieved the maximum efficiency of 96.95 % and the California Energy Commission weighted efficiency of 95.78 % when $V_L = 45$ V and the phase was adjusted. The measured efficiency with phase adjustment is much higher than that without phase adjustment because the instantaneous reactive power is fully compensated by applying the right amount of phase shift; therefore, the reactive current does not occur. Fig. 20 shows the power loss distribution of the proposed converter operating in the backward direction at full load. It shows that the primary switch power loss occupies 30.40 % and the secondary switch power loss occupies 36.50 % of the total power loss.

Using a similar number of active switches, topologies presented in [7], [8], [17], [18] achieved the bidirectional power transfer. To show the strength of the proposed converter over conventional converters, we compared them with the proposed converter in terms of topology, current waveform, the number of components, voltage balancing ability, etc. (Table II). The flyback bidirectional converters introduced in [7], [8] require the same or smaller number of active power components than the proposed converter, but they suffer serious reverse-recovery and electromagnetic interference problems when they operate with extremely high duty ratio for high voltage conversion. The current-fed half-bridge/full-bridge converters [17], [18] operate as a boost converter in the forward mode and as a buck converter in the backward mode. The magnetizing current can flow through the transformer in both directions; this trait increases the utilization of the transformer and lowers the size of the transformer. However, it requires additional boost inductors at the input side and the same or larger number of active power components. Furthermore, they experience high voltage stress on the upper capacitor of the primary side and on one of the capacitors of the secondary side. It also causes high voltage stress on the primary and secondary side switches, which in turn

TABLE II
COMPARISON OF CONVENTIONAL CONVERTERS AND PROPOSED CONVERTER

Configurations		[7, 8]	[17]	[18]	Proposed converter
Topology		Active clamp flyback	Current-fed half-bridge + half-bridge	Current-fed half-bridge + full-bridge	Dual-resonant active clamp + active-voltage -doubler
Inductor current	Forward	Linear / Resonant	Resonant	Linear	Resonant
	Backward	Linear / Resonant	Resonant	Linear	Resonant
Number of components	Switches	3 / 2	4	6	4
	Diodes	0 / 2	0	0	0
	Capacitors	3 / 4	6	2	3
	Inductors	0 / 2	3	2	1
	Transformer windings	3 / 2	-	2	2
Input voltage		24 V / 24 V	48 V	12 V	45 V
Output voltage		12 V / 110 V	380 V	288 V	380 V
Switching frequency		60 kHz / 100 kHz	105 kHz / 140 kHz	100 kHz	50 kHz
Rated power		50 W / 50 W	350 W	500 W	400 W
Peak Efficiency	Forward	85 % / 91.6 %	95.5 %	95.8 %	96.9 %
	Backward	N/A / N/A	95 %	N/A	96.9 %
Voltage balancing		-	Unbalanced	Unbalanced	Balanced

requires high power rating components, thereby increasing the circuit size and implementation cost. Compared to [17], [18], the proposed converter achieves a high conversion ratio with balanced capacitor voltage. Also, by applying the right amount of phase, it transfers power without instantaneous reactive power in both power flow directions. Moreover, it needs a relatively larger size transformer but not additional boost inductors.

VI. CONCLUSION

This article presents bidirectional operation of the resonant converter with balanced capacitor voltage. When transferring power in the backward direction, the resonant converter with balanced capacitor voltage may suffer from significant instantaneous reactive power due to synchronous rectification and large capacitor voltage fluctuation. By applying the right amount of phase to the PWM signal, we can transfer power in the backward direction without any noticeable reactive power. The nominal duty ratio of the secondary side is derived first in terms of the backward voltage gain, and then the threshold load is derived, above which the instantaneous reactive power begins to appear and the required amount of phase shift is computed to remove this reactive power. Compared to the conventional bidirectional converters, the proposed converter can be built with a reduced number of power components and with a high voltage conversion ratio and balanced capacitor voltage. To confirm the validity of the proposed converter, a 400-W prototype converter was built and its expected performance is demonstrated.

REFERENCES

[1] "U.S. battery storage market trends," U.S. Energy Information Administration, May 2018.

[2] J. Huang, J. Xiao, C. Wen, P. Wang, and A. Zhang, "Implementation of bidirectional resonant dc transformer in hybrid ac/dc micro-grid," *IEEE Trans. Smart Grid*, vol. 10, no. 2, pp. 1532–1542, Mar. 2019.

[3] Y. Xia, W. Wei, Y. Peng, P. Yang, and M. Yu, "Decentralized coordination control for parallel bidirectional power converters in a grid-connected DC microgrid," *IEEE Trans. Smart Grid*, vol. 9, no. 6, pp. 6850–6861, Jul. 2017.

[4] S. G. Jeong, J. M. Kwon, and B. H. Kwon, "High-efficiency bridgeless single-power-conversion battery charger for light electric vehicles," *IEEE Trans. Ind. Electron.*, vol. 66, no. 1, pp. 215–222, Aug. 2018.

[5] Y. C. Hsu, S. C. Kao, C. Y. Ho, P. H. Jhou, M. Z. Lu, and C. M. Liaw, "On an electric scooter with G2V/V2H/V2G and energy harvesting functions," *IEEE Trans. Power Electron.*, vol. 33, no. 8, pp. 6910–6925, Aug. 2018.

[6] G. Chen, Y. S. Lee, S. Y. R. Hui, D. Xu, and Y. Wang, "Actively clamped bidirectional flyback converter," *IEEE Trans. Ind. Electron.*, vol. 47, no. 4, pp. 770–779, Aug. 2000.

[7] H. S. H. Chung, W. L. Cheung, and K. S. Tang, "A ZCS bidirectional flyback dc/dc converter," *IEEE Trans. Power Electron.*, vol. 19, no. 6, pp. 1426–1434, Nov. 2004.

[8] M. Delshad, N. A. Madiseh, and M. R. Amini, "Implementation of soft-switching bidirectional flyback converter without auxiliary switch," *IET Power Electron.*, vol. 6, no. 9, pp. 1884–1891, Nov. 2013.

[9] C. L. Shen, H. Liou, T. C. Liang, and H. Z. Gong, "An isolated bidirectional interleaved converter with minimum active switches and high conversion ratio," *IEEE Trans. Ind. Electron.*, vol. 65, no. 3, pp. 2313–2321, Mar. 2018.

[10] L. Huang, Z. Zhang, and M. A. E. Andersen, "Analytical switching cycle modeling of bidirectional high-voltage flyback converter for capacitive load considering core loss effect," *IEEE Trans. Power Electron.*, vol. 31, no. 1, pp. 470–487, Jan. 2016.

[11] P. Thummala, D. Maksimovic, Z. Zhang, and M. A. E. Andersen, "Digital control of a high-voltage (2.5 kV) bidirectional dc–dc flyback converter for driving a capacitive incremental actuator," *IEEE Trans. Power Electron.*, vol. 31, no. 12, pp. 8500–8516, Dec. 2016.

[12] F. Z. Peng, H. Li, G.-J. Su, and J. S. Lawler, "A new ZVS bidirectional dc-dc converter for fuel cell and battery application," *IEEE Trans. Power Electron.*, vol. 19, no. 1, pp. 54–65, Jan. 2004.

[13] D. Liu and H. Li, "A ZVS bi-directional dc-dc converter for multiple energy storage elements," *IEEE Trans. Power Electron.*, vol. 21, no. 5, pp. 1513–1517, Sep. 2006.

[14] L. Wang, Z. Wang, and H. Li, "Asymmetrical duty cycle control and decoupled power flow design of a three-port bidirectional dc-dc converter for fuel cell vehicle application," *IEEE Trans. Power Electron.*, vol. 27, no. 2, pp. 891–904, Feb. 2012.

[15] S. Samanta, A. K. Rathore, and D. J. Thrimawithana, "Bidirectional current-fed half-bridge (C) (LC)–(LC) configuration for inductive wireless power transfer system," *IEEE Trans. Ind. Appl.*, vol. 53, no. 4, pp. 4053–4062, Jul./Aug. 2017.

[16] K. C. Tseng, S. Y. Chang, and C. A. Cheng, "Novel isolated bidirectional interleaved converter for renewable energy applications," *IEEE Trans. Ind. Electron.*, vol. 66, no. 12, pp. 9278–9287, Dec. 2019.
[17] A. K. Rathore, D. R. Patil, and D. Srinivasan,"Non-isolated bidirectional soft-switching current-fed LCL resonant dc/dc converter to interface energy storage in DC microgrid," *IEEE Trans. Ind. Appl.*, vol. 52, no. 2, pp. 1711–1722, Mar./Apr. 2016.
[18] A. K. Rathore and U. R. Prasanna, "Analysis, design, and experimental results of novel snubberless bidirectional naturally clamped ZCS/ZVS current-fed half-bridge dc/dc converter for fuel cell vehicles," *IEEE Trans. Ind. Electron.*, vol. 60, no. 10, pp. 4482–4491, Oct. 2013.
[19] X. Pan, H. Li, Y. Liu, T. Zhao, C. Ju, and A. K. Rathore, "An overview and comprehensive comparative evaluation of current-fed-isolated-bidirectional dc/dc converter," *IEEE Trans. Power Electron.*, vol. 35, no. 3, pp. 2737–2763, Mar. 2020.
[20] S. Son, O. A. Montes, A. J. Ferre, and M. Kim, "High step-up resonant dc/dc converter with balanced capacitor voltage for distributed generation systems," *IEEE Trans. Power Electron.*, vol. 34, no. 5, pp. 4375–4387, May 2019.
[21] M. Li, C. K. Tse, and X. Ma, "Calculation of steady-state solution of parallel-connected buck converters with active current sharing and its parameter sensitivity," *Int. J. Circ. Theor. Appl.*, vol. 39, no. 3, pp. 275–297, Mar. 2011.
[22] S. Bolognani, L. Peretti, and M. Zigliotto, "Parameter sensitivity analysis of an improved open-loop speed estimate for induction motor drives," *IEEE Trans. Power Electron.*, vol. 23, no. 4, pp. 2127–2135, Jul. 2008.
[23] J. J. Lee, J. M. Kwon, E. H. Kim, and B. H. Kwon, "Dual series-resonant active-clamp converter," *IEEE Trans. Ind. Electron.*, vol. 55, no. 2, pp. 699–710, Jan. 2008.

Sungho Son (Member, IEEE) was born in Seongnam, South Korea, in 1989. He received the B.S. degree in electrical engineering and the Ph.D. degree in creative IT engineering (CiTE) from the Pohang University of Science and Technology (POSTECH), Pohang, South Korea, in 2012 and 2019, respectively.

In 2019, he was a Senior Researcher with the Agency for Defense Development (ADD), Daejeon, South Korea. Since 2019, he has been a Power Electronic Engineer with the Coil Power Supply Section, ITER Organization, Saint Paul lez-Durance, France. His research interests include thermonuclear fusion, renewable energy system, and controller design for power systems.

Hwasoo Seok (Student Member, IEEE) was born in Incheon, South Korea, in 1993. He received the B.S. degree in electrical engineering in 2015 from the Pohang University of Science and Technology (POSTECH), Pohang, Korea, where he is currently working toward the Ph.D. degree in creative IT engineering.

His research interests include power conversion systems and control, fuel-cell converters, and bidirectional converters.

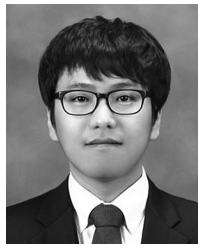

Minsung Kim (Member, IEEE) was born in Ulsan, Korea, in 1986. He received the B.S. and Ph.D. degrees in electrical engineering from the Pohang University of Science and Technology (POSTECH), Pohang, Korea, in 2008 and 2013, respectively.

Since 2013, he has been with the Department of Creative IT Engineering and Future IT Research Laboratory, POSTECH, Pohang, Korea, where he was a Research Assistant Professor. In 2016, he was a Research Scholar with Future Energy Electronics Center, Virginia Tech, Blacksburg, VA, USA. From 2017 to 2018, he has also served as an Academic Visitor with Control and Power System Group, Imperial College London, London, U.K. Since 2018, he has been with the Division of Electronics and Electrical Engineering, Dongguk University, Seoul, Korea, where he is currently an Assistant Professor. His current research interests include highly efficient power conversion circuit design, intelligent controller design for industrial electronics, renewable energy, and energy storage systems.